The final publication is available at

http://doi.org/10.1088/1361-6528/aa6a3f

Additional Information

Structural and Vibrational Properties of Corundum-type In$_2$O$_3$ Nanocrystals under Compression

J.A. Sans,[1,*] R. Vilaplana,[2] D. Errandonea,[3] V.P. Cuenca-Gotor,[1] B. García-Domene,[3] C. Popescu,[4] F. J. Manjón,[1] A. Singhal,[5] S. N. Achary,[5] D. Martinez-Garcia,[3] J. Pellicer-Porres,[3] P. Rodríguez-Hernández,[6] and A. Muñoz [6]

[1] Instituto de Diseño para la Fabricación y Producción Automatizada, MALTA Consolider Team-Universitat Politècnica de València, 46022 València, Spain

[2] Centro de Tecnologías Físicas: Acústica, Materiales y Astrofísica, MALTA Consolider Team, Universitat Politècnica de València, 46022 València, Spain

[3] Departamento de Física Aplicada-ICMUV, MALTA Consolider Team, Universidad de Valencia, Edificio de Investigación, C/Dr. Moliner 50, Burjassot, 46100 Valencia, Spain

[4] ALBA-CELLS, Cerdanyola, 08290 Barcelona, Spain

[5] Chemistry Division, Bhabha Atomic Research Centre, Trombay, Mumbai 400085, India

[6] Departamento de Física, Instituto de Materiales y Nanotecnología, MALTA Consolider Team, Universidad de La Laguna, 38205 Tenerife, Spain

E-mail: juasant2@upv.es

ABSTRACT

This work reports the structural and vibrational properties of nanocrystals of corundum-type In$_2$O$_3$ (rh-In$_2$O$_3$) at high pressures by using angle-dispersive x-ray diffraction and Raman scattering measurements up to 30 GPa. The equation of state and the pressure dependence of the Raman-active modes of the corundum phase in nanocrystals are in good agreement with previous studies on bulk material and compare nicely with theoretical simulations on bulk rh-In$_2$O$_3$. Nanocrystalline rh-In$_2$O$_3$ showed stability under compression at least up to 20 GPa, unlike bulk rh-In$_2$O$_3$ which gradually transforms to the orthorhombic *Pbca* (Rh$_2$O$_3$-III-type) structure above 12-14 GPa. The different stability range found in nanocrystalline and bulk In$_2$O$_3$ is discussed.

1. Introduction

Indium oxide (In$_2$O$_3$) is a sesquioxide whose stable phase at room conditions is the cubic bixbyite-type structure[1] (space group (SG) *Ia-3*, N. 206, Z=16). This phase has been widely studied for optoelectronic applications due to its special properties as a transparent conducting oxide (TCO).[2,3] The widespread use of cubic In$_2$O$_3$ (c-In$_2$O$_3$) in industrial processes covers the

fabrication of window layers in solar cells,[3-5] light-emitting diodes,[6,7] electrochromic windows,[8] liquid-crystal displays,[9,10] and gas sensors.[11,12] However, the scarcity and high cost to obtain indium metal has led to the study of new systems, like Sn-doped In_2O_3 (ITO) and $In_{2-2x}Zn_xSn_xO_3$ ($x \leq 0.4$, also named ZITO or IZTO), in order to cut the price of its production process.[13-15]

Rhombohedral corundum-type (SG *R-3c*, N. 167, Z= 6) In_2O_3 is also known to be a metastable phase at room conditions that can be obtained after high pressure (HP)-high temperature (HT) treatment, but also at room pressure.[16-40] Modern calculations of pure and doped rhombohedral In_2O_3 (rh-In_2O_3), suggest that this phase could be even better TCO than c-In_2O_3; thus opening a new way to search for improved TCOs.[41-44]

Given the above result, it is clear that the study of the HP phases (perhaps metastable at ambient conditions) of a technological important compound, like In_2O_3, is crucial for the advancement of science and technology.[45-47] In this respect, three additional orthorhombic phases of In_2O_3 have been theoretically predicted and indeed obtained by application of HP: Rh_2O_3-III type (SG *Pbca*, N. 61, Z= 8),[36,37] Rh_2O_3-II type (SG *Pbcn*, N. 60, Z= 4),[32, 48-51] and α-Gd_2S_3-type (SG *Pnma*, N. 62, Z= 4).[52] Among them only the *Pbcn* phase has been claimed to be metastable at ambient conditions,[49-51] despite the *Pbca* phase is a phase reported at lower pressures than the *Pbcn* phase.[36,37]

Working with nanocrystals opens the door to enhanced properties of materials;[53,54] and adds the possibility of obtaining metastable HP crystalline and amorphous phases at room conditions with different properties from the original material.[47,55-57] It is well known that most nanocrystals undergo a pressure-induced phase transition at larger pressures than in the bulk and that many nanocrystals undergo a pressure-induced amorphization;[55] however, many questions remain open regarding the behaviour of nanocrystals at HP in comparison with bulk materials. In

particular, the different thermodynamic stability of crystalline phases in nanocrystals as compared to bulk material,[55,56] and whether the compressibility of nanocrystals is different to that of bulk material or if the different compressibility comes from a different degree of hydrostaticity affecting micro and nanocrystal powders.

Even if several works have been devoted to the study of In_2O_3 nanocrystals at HP, most of them have focused on nanocrystals of cubic bixbyite-type In_2O_3,[58-60] and only a small part have been devoted to study nanocrystals of rhombohedral corundum-type In_2O_3.[49,50,59] In fact, a different stability range of the rhomobohedral phase under compression has been observed depending on the sample size. Gurlo et al., who studied nanocrystals of rh-In_2O_3, suggested that this compound is stable at room temperature between room pressure and 30 GPa;[49] however, two recent studies reported that bulk rh-In_2O_3 undergoes a transformation above 12-14 GPa in good agreement with theoretical simulations.[36,37] The apparent lack of phase transition in nanocrystals up to 30 GPa suggests the existence of large kinetic barriers to explain their extended structural stability.

In this work we report a HP study of the structural and vibrational properties of nanocrystals of corundum-type In_2O_3 by means of angle-dispersive powder x-ray diffraction (XRD) and Raman scattering (RS) measurements up to 30 GPa. Both the equation of state and the pressure dependence of the Raman-active modes of the corundum phase in nanocrystals are reported, showing a nice agreement with previous studies on rh-In_2O_3 nanocrystals.[49] These results have been compared with experimental and theoretical structural and lattice dynamics results on bulk rh-In_2O_3 offering an explanation to the previously apparent contradicting results observed between bulk and nanocrystalline rh-In_2O_3.

2. Methods

2.1. Experimental details

Rh-In$_2$O$_3$ nanoparticles were synthesized by thermal dehydration of InOOH nanoparticles previously prepared from a solvothermal reaction between indium nitrate and tetramethylammonium hydroxide.[61] XRD measurements confirm that nanocrystalline powders are pure and have corundum-type structure with an hexagonal unit cell with lattice parameters $a=b=$ 5.485 Å and $c=$ 14.530 Å, which are in good agreement with reference JCPDS card 220336 ($a=b=$ 5.487 Å and $c=$ 14.510 Å). On the other hand, transmission electron microscopy (TEM) confirmed both the crystalline structure and purity and determined that nanocrystals have a rice-grain type morphology with an average length (width) of 20 (13) nm and a uniform distribution between 10 (6) and 30 (20) nm.[61] Room-temperature experiments in rh-In$_2$O$_3$ nanocrystals were conducted up to 30 GPa in a membrane-type diamond anvil cell. In HP-XRD and HP-RS experiments, powder sample was loaded inside a 150 μm diameter hole drilled in an inconel gasket together with a mixture of methanol-ethanol-water (MEW) in a 16:3:1 proportion as a quasi-hydrostatic pressure-transmitting medium (PTM) as in a previous work,[37] in order to compare results for bulk and nanocrystalline rh-In$_2$O$_3$ under the same conditions. Additionally, a second XRD experiment with Ar as PTM was done in order to prove if nanopowders could be affected by non-hydrostatic effects using MEW and to compare with previous results described in the literature.[37] For pressure calibration in angle-dispersive powder XRD and RS measurements we introduced inside the pressure cavity Cu powder[62] and ruby,[63] respectively. In the XRD experiments we collected also two patterns, one in the region where the Cu peaks were strong and the other where there is no Cu signal. The first pattern was used to determine pressure and the second one to analyse the crystal structure of In$_2$O$_3$.

Angle-dispersive powder XRD measurements at different pressures were performed in the MSPD beamline[64] at ALBA synchrotron facility. This beamline is equipped with Kirkpatrick-Baez mirrors to focus the monochromatic beam and a SX165 CCD detector with a diameter of 165 mm. We used a wavelength of 0.4246 Å and the sample-detector distance during the experiment was set to 240 mm. The 2-D diffraction images were integrated with FIT2D software.[65] Lattice parameters of XRD patterns were obtained with Rietveld refinements performed using POWDERCELL[66] and GSAS[67] program packages. On the other hand, RS measurements at room temperature and different pressures were excited using the 632.8 nm HeNe laser (with a power below 10 mW) and collected in backscattering geometry with a Horiba Jobin Yvon LabRam HR UV spectrometer equipped with a thermoelectrically cooled multichannel CCD detector (resolution below 2 cm^{-1}).

2.2. Theoretical Calculations

Total-energy *ab initio* calculations were performed for bulk rh-In$_2$O$_3$ within the density functional theory (DFT)[68] using the Vienna *Ab initio* Simulation Package (VASP)[69] as described in Ref. 37 for bulk rh-In$_2$O$_3$. In particular, we have used the projector-augmented wave (PAW)[70] scheme implemented in this package and the generalized gradient approximation (GGA) was used for the description of the exchange-correlation energy with the PBEsol prescription.[71]

We have also performed lattice dynamics calculations of the phonon modes in bulk rh-In$_2$O$_3$ at the center of the BZ (Γ point) using the direct force constant approach (or supercell method)[72] already described in Ref. 37. Our theoretical results provide both the frequencies of the normal modes and their polarization vectors and enable us to assign the Raman-active modes observed in nanocrystalline rh-In$_2$O$_3$ as previously done for bulk rh-In$_2$O$_3$.[37]

3. Results

3.1. XRD measurements

Figure 1a shows a selection of the experimental angle-dispersive powder XRD patterns of rh-In_2O_3 at room temperature at different pressures up to 21 GPa obtained in the first experiment (using MEW mixture as PTM). **Figure 1b** shows similar results up to 29.8 GPa obtained in the second experiment (using Ar as PTM). All the XRD patterns can be indexed with the corundum-type structure. Under compression some of the peaks shift faster to higher angles than others due to the anisotropic compressibility of In_2O_3 which will be discussed in detail later. This phenomenon is illustrated in **Figs. 1a and 1b** by the (104) and (110) Bragg peaks which gradually merge under compression because the interplanar distance associated to the (104) peak decreases faster under compression than that corresponding to the (110) reflection. In the second experiment, in addition to the Bragg peaks of the sample, Bragg peaks of Ar are also detected. These peaks can be easily identified because, due to the large compressibility of Ar, they shift faster to higher angles under compression than the peaks corresponding to In_2O_3. The Ar peaks were used to confirm the pressure determined from Cu using the equation of state of Ar.[73] The pressure determined from Ar agrees within 0.1 GPa with the pressure determined from Cu. The results of both XRD experiments indicate that the phase transition to the *Pbca*-type phase observed in bulk rh-In_2O_3 above 12-14 GPa,[36,37] is not observed in nanocrystals even at 29.8 GPa. We would like to comment here that beyond 20 GPa all the peaks assigned to corundum-type In_2O_3 can be also explained with the *Pbca*-type structure. However, this structure has a peak at low angles, the (002) peak expected to be located around 3.2º, which is not present in the corundum-type structure. In our experiments, we did not observe this peak, which supports the stability of the corundum-type structure up to

29.8 GPa. This result is in agreement with the larger stability of the corundum phase measured by Gurlo et al. in nanocrystalline rh-In_2O_3 samples with particle size between 50 and 100 nm.[49] XRD peaks in our first experiment show slight broadening with increasing pressure above 10 GPa which could be due to a slight loss of quasi-hydrostatic conditions of the PTM. The same broadening is observed in the second experiment but around 20 GPa. This is a consequence of the better quasi-hydrostatic conditions generated by Ar than by MEW above 10 GPa.[74] In this regard, it is expected that small non-hydrostatic stresses do not influence the structural stability of relatively uncompressible compounds like sesquioxides.[75]

In this work, we have extracted the evolution of the structural parameters of nanocrystalline rh-In_2O_3 under compression by Rietveld refinement. In **Figure 1**, one can see the experimental diffraction pattern (black symbols), the Rietveld refinement performed (black line) and the residuals (red lines) showing a good fit to the experimental data. **Figure 2** represents the experimental pressure dependence of the hexagonal unit-cell volume, lattice parameters a and c and the c/a ratio in nanocrystalline rh-In_2O_3. The experimental data of the unit-cell volume up to 29.8 GPa can be fitted with a third-order Birch-Murnaghan (BM) EOS,[76,77] which yields V_0= 376.7(4) A^3, B_0= 169(6) GPa and B_0'= 6.2(9). These values are in good agreement with theoretical data of bulk material fitted up to 30 GPa (V_0= 383.3 A^3, B_0= 169 GPa and B_0'= 3.3) and with previous experimental (B_0= 176-180 GPa) and theoretical estimations in bulk material.[37] Note that the value of the bulk modulus for rh-In_2O_3 nanocrystals is slightly smaller than that in bulk material (see **Table I**). In relation to this, it must be noted that a decrease of the bulk modulus in nanocrystals with respect to bulk material has been observed in a number of oxides, like TiO_2,[78,79] ZrO_2,[80,81] SnO_2,[82] MgO,[83] ZnO,[84] and Al_2O_3.[85]

A deviation of the compressibility of nanocrystals above certain pressure has been found in other works. In particular, nanocrystals of anatase TiO_2 pressurized with a 4:1 methanol-ethanol mixture were found to undergo deviations of the compressibility of the *a* axis and unit-cell volume above 10-12 GPa which were attributed to the appearance of an intermediate local distortion (~ 2 Å) with TiO_2-II structure.[86] On the other hand, a significantly lower bulk modulus (148±5 GPa) compared to theoretical calculations (169.4 GPa) has been recently observed in c-In_2O_3 nanocrystals with a high defect density under compression with a 4:1 methanol-ethanol mixture as PTM.[60] In that work, authors claimed that the different bulk modulus of two nanocrystalline samples with similar sizes and morphologies were due to their different defect densities. Another possibility is that the change in compressibility observed above 8 GPa in In_2O_3 nanocrystals could be due to non-hydrostatic conditions as it was reasoned for nanocrystalline TiO_2 anatase.[78] Note that nanocrystalline powder is more prone to non-hydrostatic conditions than bulk powder because the surface area of nanocrystalline grains tend to be more surrounded by other nanocrystalline grains than by the molecules of the PTM. On the other hand, the surface area of microcrystalline grains tend to be more surrounded by the molecules of the PTM than by other grains. In any case, it was demonstrated for nanocrystalline TiO_2 anatase that the EOS obtained prior to observation of non-hydrostatic conditions is in good agreement with the EOS obtained under truly hydrostatic conditions along the whole range of the experiments.[78] Since measurements in nanocrystalline rh-In_2O_3 using MEW or Ar show similar results (see **Fig. 2**), we are confident of the bulk modulus obtained for nanocrystals with an average grain size around 20 nm up to 30 GPa. It must be stressed that the bulk modulus we have obtained for rh-In_2O_3 nanocrystals in the present study is much smaller than that reported (305 GPa) in a previous work.[58] In fact, Ref. 58 also reports an overestimation of the bulk modulus in rh-In_2O_3 as was also confirmed in our previous work.[37] The

main reason for the overestimation of the bulk modulus in Ref. 58 is the lack of structural data for the corundum-type phase at low pressures and the inherent uncertainty caused by the extrapolation of the bulk modulus from data above 20 GPa.

On the other hand, both a and c lattice parameters show a rather similar pressure dependence in both bulk material and nanocrystals, also observed in the c/a ratio (inset of **figure 2b**). The lattice parameters of rh-In_2O_3 nanocrystals show an almost linear variation with pressure. Both a and c parameters have been fitted to a modified Murnaghan's equation with free parameters a_0, B_0 and B_0'.

$$a = a_0 \left(1 + \frac{B_0'}{B_0}P\right)^{-\left(\frac{1}{3B_0'}\right)} \quad , \qquad \text{Eq. (1)}$$

The results of these fits are shown in **Table II**. The axial compressibilities of the a- and c-axis defined as $\kappa_x = \frac{-1}{x}\frac{\partial x}{\partial P}$ (where $x = a, c$) can be obtained as $\kappa_x = \frac{1}{3B_0}$ with the B_0 values obtained with the Murnaghan EOS fit for the lattice parameters. The experimental compressibility of the a (c) axis is 1.4 (3.0) $\cdot 10^{-3}$ GPa^{-1} This result indicates that the c axis is more than two times more compressible than the a axis as it occurs in bulk rh-In_2O_3.[37] Consequently, we can conclude that the major contribution to the compressibility of nanocrystalline rh-In_2O_3 comes from the larger compressibility of the c axis than that of the a axis. These behaviours are in agreement with experiments and theoretical calculations already published for bulk rh-In_2O_3[37] and theoretical calculations (Table II). Similarly, the c/a ratio in bulk and nanocrystalline rh-In_2O_3 shows the same tendency in good agreement with our theoretical calculations; however, this behaviour is different to that reported in corundum-type Al_2O_3, V_2O_3, Cr_2O_3, and Fe_2O_3,[87] as already discussed in our previous work regarding bulk rh-In_2O_3.[37]

3.2. Raman scattering

The corundum structure of In_2O_3 has 7 Raman-active modes whose frequencies at ambient pressure have been already reported in bulk and nanocrystals.[22,30,37,39,40] **Figure 3** shows selected Raman spectra of nanocrystalline rh-In_2O_3 at different pressures up to 29.3 GPa using MEW as PTM. As observed, the RS spectrum of nanocrystals is dominated by the A_{1g} mode with lowest frequency (near 163 cm^{-1} at room pressure). Table III summarizes the Raman-active modes of our nanocrystals at ambient conditions compared to those found in bulk material. All Raman frequencies in nanocrystals differ by less than 10 cm^{-1} from those of the bulk material. In order to analyse the influence of the morphology of the nanocrystals in the Raman frequencies, different nanocrystalline geometries can also be compared. Hierarchical nanocrystals orderly dendrite-like aggregates[39] and 3D rh-In_2O_3 nanoflowers[40] were characterized by XRD and Raman spectroscopy at room conditions. In the former geometry, the Raman spectrum showed peaks at 164, 222, 273, 385, 504, and 595 cm^{-1} whereas in the latter, the Raman modes appeared at 163, 219, 384, 501 and 590 cm^{-1}. Regarding the XRD patterns of these samples at room conditions, both studies reported a good correlation with lattice planes obtained from the JCPDS database. It can be concluded that the difference in Raman frequency between the different geometries of rh-In_2O_3 nanocrystals is less than 5 cm^{-1}, which reveals the low influence of the morphology in the vibrational properties.

As regards the pressure dependence of the Raman-active modes, the A_{1g} mode of the corundum phase is observed up to 24.8 GPa; i.e., almost up to the same pressure as in bulk rh-In_2O_3 (26 GPa).[37] However, a slight change in the RS spectrum is observed above 21.5 GPa (more clear in the spectra at 24.8 and 29.3 GPa) with the appearance of new peaks which are coincident with the decrease of the intensity of the A_{1g} peak of the corundum phase. The new modes can be reasonably attributed to *Pbca*-type In_2O_3 (with Rh_2O_3-III structure) since the most intense mode of

this phase has a slightly larger frequency (near 183 cm^{-1}) than the A_{1g} mode of the corundum phase.[36,37] In this way, all RS modes of the sample at 29.3 GPa are attributed to the orthorhombic *Pbca* phase. Finally, in the downstroke process, the rhombohedral phase was recovered below 8 GPa (see top RS spectrum in **Fig. 4**); i.e, at a similar pressure as in bulk material.[37] Therefore, the hysteresis in rh-In$_2$O$_3$ nanocrystals is larger than in bulk material.

It is noteworthy that a HP phase transition from the corundum type phase to the *Pbca* phase is observed above 20 GPa in RS measurements, but not in XRD measurements. The explanation for this discrepancy could come from different aspects. First, it is well known that RS measurements are more sensitive to local structural changes than XRD measurements and HP phase transitions are observed at lower pressures in RS measurements than in XRD measurements.[88] In our nanocrystals, this fact could lead to the observation of the HP transition beyond 25 GPa by XRD measurements. Second, the nanometric size of samples, leading to broader XRD peaks than those in bulk material, and the fact that many peaks of the rhombohedral *R-3c* and orthorhombic *Pbca* phases are coincident in the range between 20 and 30 GPa, provides additional difficulty to the observation of the HP phase transition even beyond 25 GPa since the small peak near 3.2° could be smeared out in nanocrystals. Third, it has been recently shown that HP transformations in nanocrystals can be affected by internal defects[60] or even surface effects,[89,90] which could eventually depend on the PTM. This means that the HP phase transition measured in RS measurements using MEW could be retarded when using Ar, which will explain the lack of phase transition even up to 30 GPa in this work and on that of Gurlo et al.[49] Supporting this assumption, we already observed a similar behaviour on bulk c-In$_2$O$_3$ under compression.[36] The transition pressure from cubic-to-orthorhombic phase appeared at 35 GPa using the most hydrostatic PTM (helium), whereas using MEW was observed at slightly lower pressures (31

GPa). Finally, some transitions not observed by XRD at ambient temperature can be induced by local laser heating in small bandgap materials or in samples with dark defects which are precursors of the HP phase transition.[91] The lack of radiation damage by laser heating in rh-In_2O_3 nanocrystals is supposed by the large bandgap energy of this compound (above 3.75 eV at ambient pressure).[92] In fact, the energy bandgap of rh-In_2O_3 under compression remains in the UV region up to around 20 GPa. The origin of this controversy could be unveiled by new single crystal XRD experiments well above 20 GPa in rh-In_2O_3 nanocrystals using a nanosize beam[93] and using argon, neon or helium as PTM.

Figure 4 shows the pressure dependence of the experimental and theoretical frequencies of the first-order Raman-active modes of rh-In_2O_3 nanocrystals. All Raman-active mode frequencies increase with pressure in a monotonous way up to the maximum pressure attained in the experiment in good agreement with previously reported experimental and theoretical Raman modes for bulk rh-In_2O_3.[37] **Table III** summarizes the zero-pressure experimental and theoretical frequencies, pressure coefficients and the Grüneisen parameters of the Raman active modes of rh-In_2O_3 nanocrystals. Above 20 GPa new peaks have been attributed to the *Pbca* phase due to the similarity to previously reported RS spectrum and pressure dependences of the observed peaks. It must also be considered that different rh-In_2O_3 nanocrystals with different morphologies other than rice-grain type have been grown in the last decade.[39,40] A priori, we expect that all nanoparticles with similar size behave in a similar way.[79] In any case, future HP experiments using rh-In_2O_3 nanocrystals with different morphologies will help to understand the HP behaviour of rh-In_2O_3 nanocrystals.

Finally, we would like to stress that the higher sensitivity of rh-In_2O_3 to compression than its isostructural compounds Al_2O_3, Ga_2O_3, and Cr_2O_3 could be relevant for pressure calibration.

As commented in our previous work on bulk rh-In_2O_3,[37] the most usual method for pressure calibration in the laboratory relies on spectroscopic techniques in ruby, whose sensitivity is related to the bulk modulus of this material. Therefore, the existence of compounds with a smaller bulk modulus than ruby and with the possibility to host Cr^{3+} cations opens a new path in the search for more accurate pressure sensors. In this context, the low value of the bulk modulus of rh-In_2O_3 and the stability of the rh-In_2O_3 nanocrystals at least up to 20 GPa (8 GPa more than bulk material at least) at room temperature [37] suggest that Cr^{3+}-doped rh-In_2O_3 nanocrystals could be a possible candidate to substitute ruby at least below 20 GPa. It is expected that the higher sensitivity of the host material (rh-In_2O_3) would produce an increase of the pressure coefficient of the luminescence lines of Cr^{3+} of about 30% with respect to ruby and consequently, a more accurate determination of pressure. However, for that purpose metastable corundum-type Cr^{3+}-doped In_2O_3 nanocrystals must be prepared in an easy way as a single crystalline phase and its photoluminescence under pressure need to be studied for different concentrations of Cr^{3+} doping.
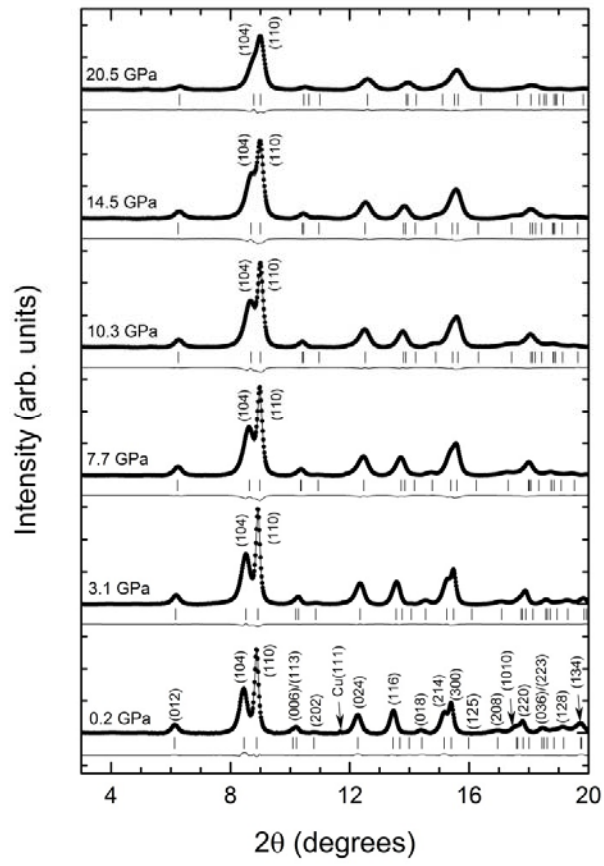
4. Conclusions

We have presented the structural and vibrational behaviour of rh-In_2O_3 nanocrystals up to 30 GPa and compared them to those of the bulk material and theoretical simulations. Angle-dispersive powder XRD measurements in rh-In_2O_3 nanocrystals have allowed us to obtain a more accurate experimental equation of state for this compound in good agreement with theoretical calculations and experiments for bulk rh-In_2O_3. Also similar pressure coefficients for the Raman-active modes have been observed in nanocrystals, thus confirming the similar bulk modulus of our nanocrystals and bulk material.

Our RS measurements confirm that rh-In$_2$O$_3$ nanocrystals undergo a phase transition towards the *Pbca* phase at much higher pressures (above 20 GPa) than in bulk material. However, such a phase transition has not been confirmed with our powder XRD measurements even up to 30 GPa. The origin of this discrepancy has been circumscribed to three possible effects, proposing a new experiment to solve it. On the downstroke, the original corundum-type phase was observed in nanocrystals below 8 GPa, as it occurs in bulk material.

Finally, it must be stressed the difference in the structural stability established between nanocrystalline and bulk rh-In$_2$O$_3$ but keeping a similar compressibility, which extends the possible applications of this compound at larger pressure ranges. Those effects are important in forthcoming studies of the possibility to use Cr^{3+}-doped rh-In$_2$O$_3$ nanocrystals at room temperature as a more sensitive pressure sensor than ruby at least up to 20 GPa.
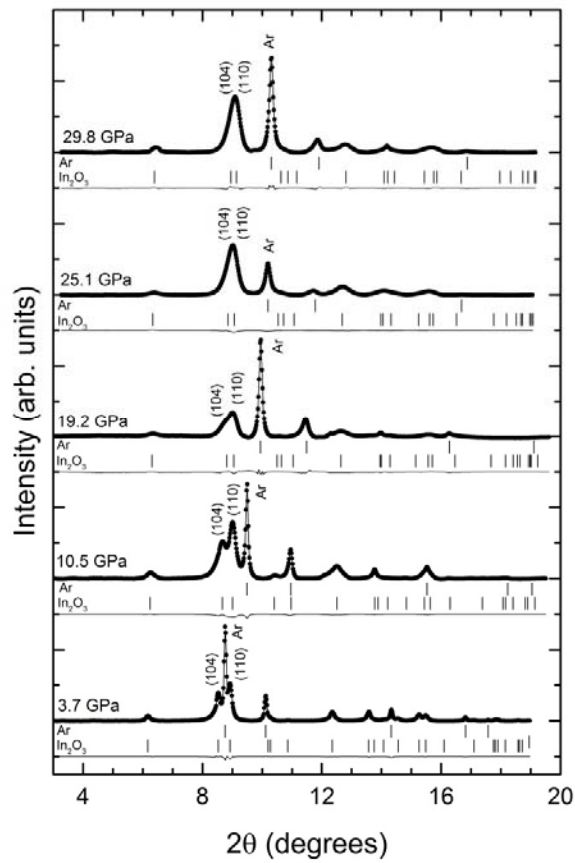
FIGURES

1a

Figure 1. Selected X-ray diffraction patterns of nanocrystalline rh-In$_2$O$_3$ at several pressures using MEW (a) and Ar (b) as PTM. Diffraction patterns have been shifted vertically for clarity. Different diffraction peaks are assigned in the graph to rh-In$_2$O$_3$ (R-3c), Ar and Cu phases. Refinements and residuals of the fit to these phases are also shown.
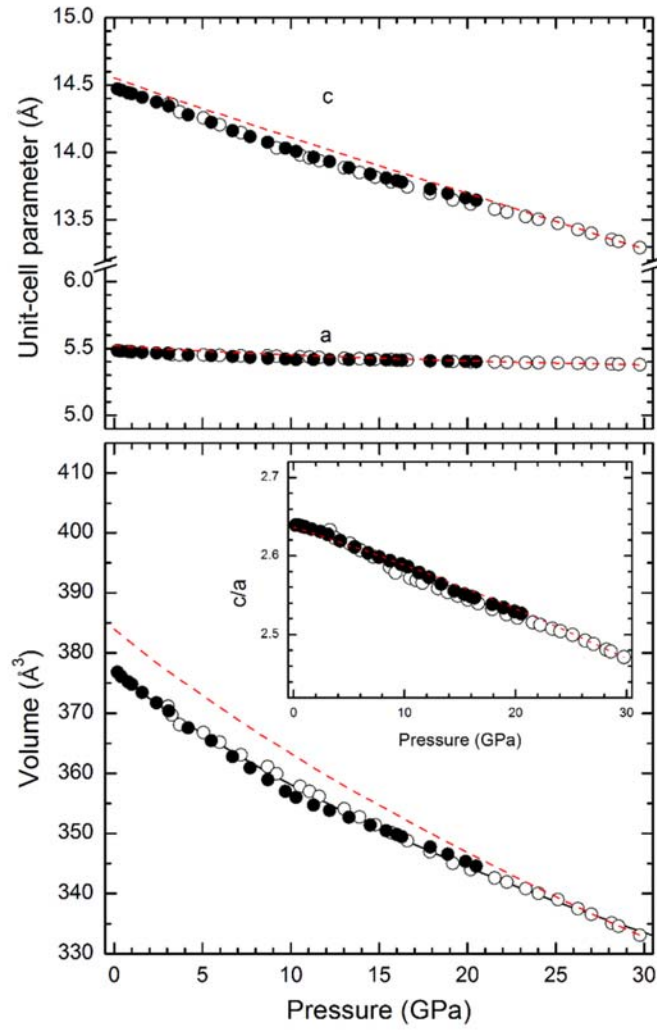
Figure 2. Pressure dependence of the unit-cell parameters **(a)** and volume **(b)** in nanocrystalline rh-In₂O₃ for our first experiment (close symbols) and the second experiment (open symbols). The inset shows the pressure dependence of the *c/a* ratio in nanocrystalline rh-In₂O₃. Red dashed lines correspond to theoretical data of bulk rh-In₂O₃.
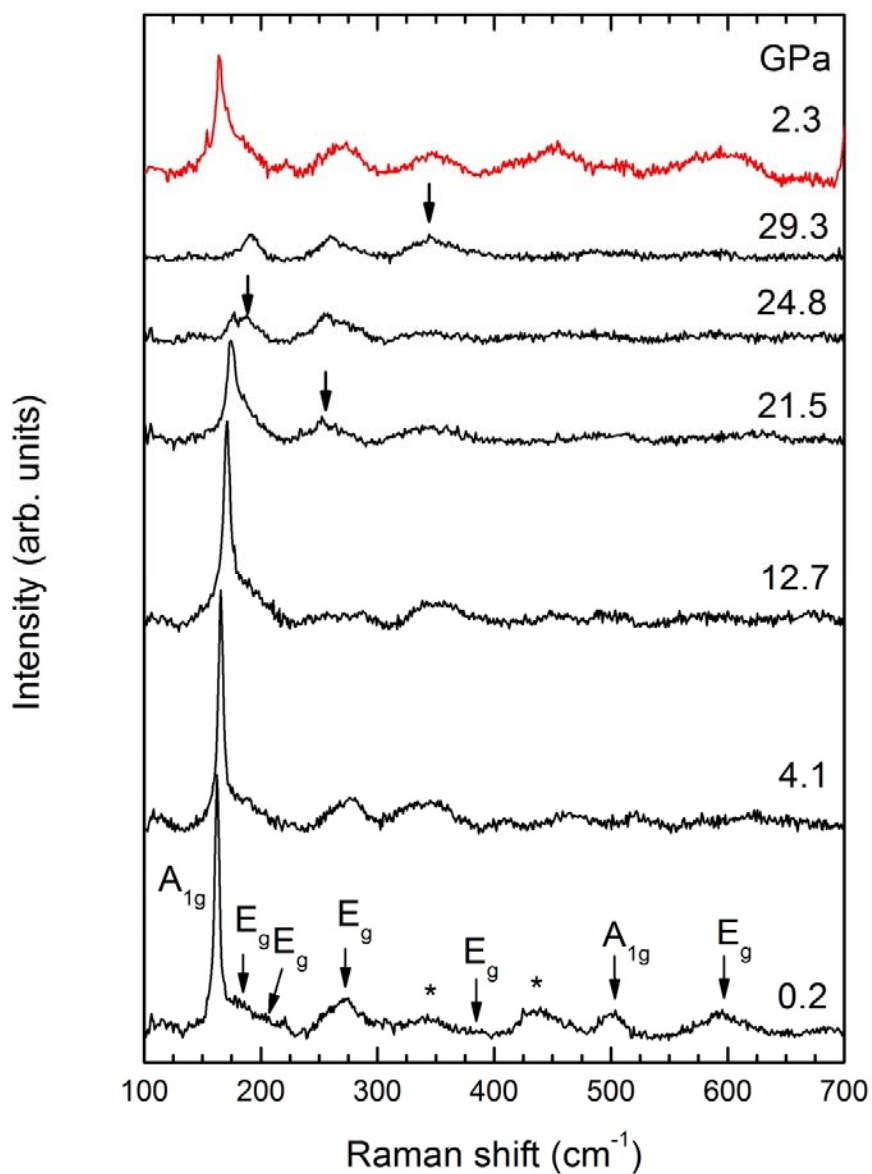
Figure 3. Selected RS spectra of nanocrystalline rh-In_2O_3 at different pressures on upstroke up to 29.3 GPa. In the RS spectrum at 0.2 GPa, first-order Raman modes of rh-In_2O_3 are indicated by arrows, while second-order Raman modes are denoted with asterisks. Above 20 GPa, arrows in the RS spectra indicate the new peaks assigned to the *Pbca* phase. The top RS spectrum at 2.3 GPa shows the reversibility of the sample to the corundum phase on downstroke.
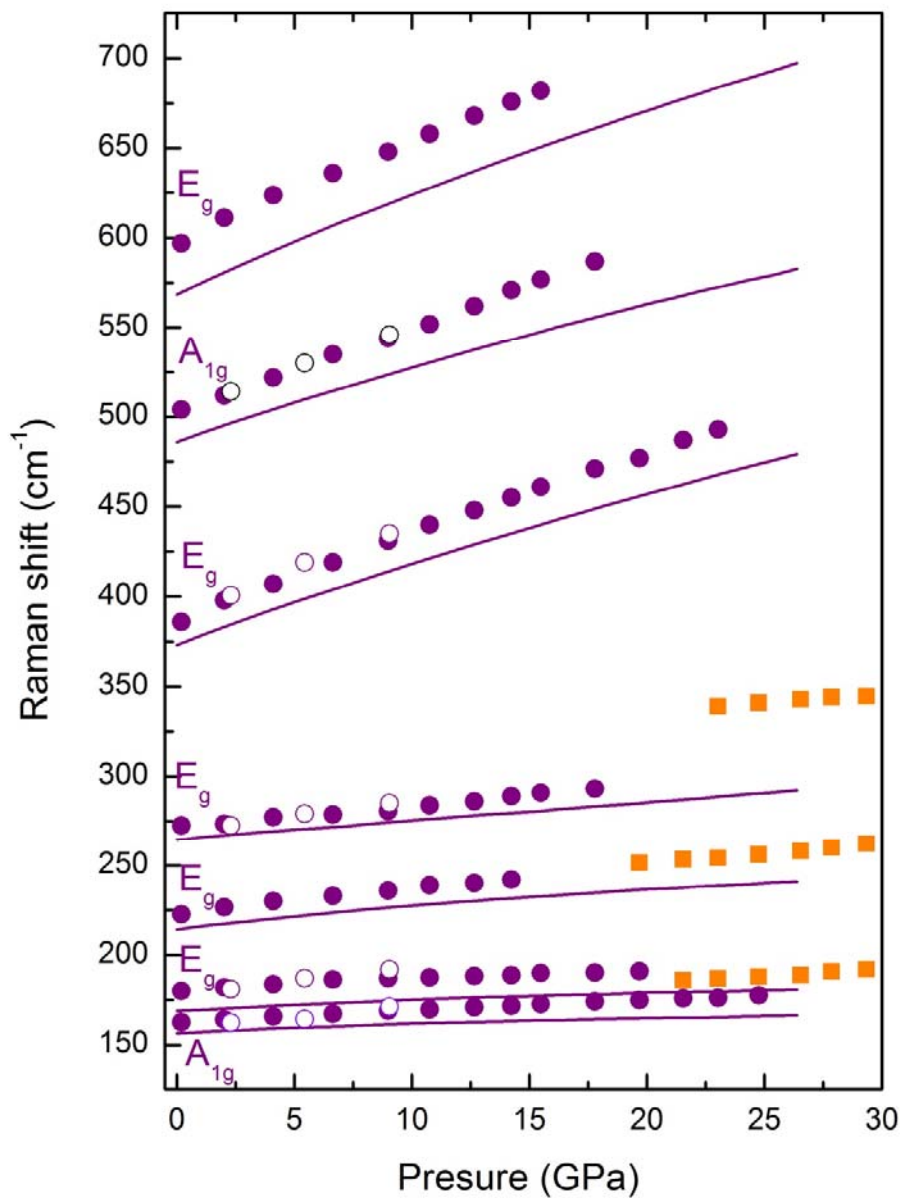
Figure 4. Pressure dependence of the Raman-active mode frequencies in nanocrystalline rh-In₂O₃ (violet circles) and *Pbca*-type In₂O₃ (orange squares). Full (empty) symbols correspond to the upstroke (downstroke) process. Solid lines correspond to *ab initio* simulated Raman-active modes of bulk rh-In₂O₃. The symmetry of the Raman-active modes of rh-In₂O₃ is indicated.

TABLES

Table I. Comparison of theoretical and experimental zero pressure unit-cell volume per formula

unit, bulk modulus, and its pressure derivative for bulk and nanocrystalline rh-In_2O_3.

	Phase	V_0 (Å^3)	B_0 (GPa)	B'_0	Method
nano	R-3c	62.78(1)	169(6)	6.2(9)	Exp. (XRD)[a]
	R-3c	61.49	305.5	2.9	Exp. (XRD)[b]
bulk	R-3c	62.86(4)	180(7)	3.2(1.2)	Exp. (XRD)[c]
	R-3c	63.88	167	3.3	Theo. (GGA-PBEsol)[d]

[a] This work
[b] Ref. 58
[c] Ref. 37
[d] Data up to 30 GPa.

Table II. Lattice parameters and their bulk modulus and pressure derivative of bulk modulus at room pressure in nanocrystalline rh-In_2O_3 (top) as compared to experimental and theoretical parameters in bulk Exp. rh-In_2O_3 (bottom)

a_0 (Å)	B_{0a} (GPa)	B_a'	c_0 (Å)	B_{0c} (GPa)	B_c'	Method
5.4831(8)	233(16)	11.8	14.461(8)	109(3)	0.48	Our Exp. (XRD)
5.479(2)	220(30)	11.8	14.511(5)	121(7)	0.48	Exp. (XRD)
5.520(1)	216(3)	11.8(4)	14.552(1)	106.0(9)	0.48(11)	Theo. (GGA-PBEsol)

Table III. Room-pressure experimental frequencies, pressure coefficients and Grüneisen parameters of the Raman active modes of bulk and nanocrystalline rh-In_2O_3.

Mode (Sym)	Bulk rh-In_2O_3								Nano rh-In_2O_3		
	Ab initio calculations				Experimental [b]				Experimental		
	ω_0 (cm^{-1})	$\dfrac{\partial\omega}{\partial P}$ $\left(\dfrac{cm^{-1}}{GPa}\right)$	$\dfrac{\partial^2\omega}{\partial P^2}$ $\left(\dfrac{cm^{-1}}{GPa^2}\right)$	γ^a	ω_0 (cm^{-1})	$\dfrac{\partial\omega}{\partial P}$ $\left(\dfrac{cm^{-1}}{GPa}\right)$	$\dfrac{\partial^2\omega}{\partial P^2}$ $\left(\dfrac{cm^{-1}}{GPa^2}\right)$	γ	ω_0 (cm^{-1})	$\dfrac{\partial\omega}{\partial P}$ $\left(\dfrac{cm^{-1}}{GPa}\right)$	γ^c
A_{1g}	156(1)	0.65 (3)	-0.012 (2)	0.66	162.3 (2)	0.85 (4)	-0.015 (1)	0.93	163.2(2)	0.590(14)	0.61
E_g	169(1)	0.73 (3)	-0.010 (2)	0.68	177.1 (2)	1.01 (6)	-0.022 (3)	1.01	181.3(5)	0.54(4)	0.50
E_g	214(1)	1.54 (3)	-0.023 (2)	1.14	218.1 (3)	1.85 (8)	-0.039 (5)	1.50	223.9(5)	1.30(3)	0.97
E_g	265(1)	1.11 (6)	-0.005 (5)	0.66	270.7 (4)	1.33 (13)	-0.011 (7)	0.87	270(1)	1.49(11)	0.93
E_g	373(2)	4.91 (5)	-0.040 (4)	2.08	383.8 (6)	4.69 (16)	-0.022 (8)	2.16	388.3(9)	4.61(6)	2.0
A_{1g}	486(2)	4.46 (6)	-0.033 (4)	1.45	501.9 (9)	3.92 (25)	0.005 (14)	1.38	502.5(6)	4.75(5)	1.6
E_g	569(2)	6.14 (5)	-0.059 (4)	1.70	590.3 (6)	5.95 (18)	-0.058 (12)	1.78	599(1)	5.42(11)	1.53

[a] Theoretical B_0= 158 GPa used for calculating the Grüneisen parameter.

[b] From ref. 37 (experimental B_0= 177 GPa used for calculating the Grüneisen parameter).

[c] Experimental B_0= 169 GPa used for calculating the Grüneisen parameter.

Author Contributions

The manuscript was written through contributions of all authors. All authors have given approval to the final version of the manuscript.

Acknowledgments

References

1   Marezio M 1966 Refinement of the Crystal Structure of In_2O_3 at two Wavelengths *Acta Crystallogr.* **20** 723-728.

2   Mizoguchi H and Woodward P M 2004 Electronic Structure Studies of Main Group Oxides Possessing Edge-Sharing Octahedra: Implications for the Design of Transparent Conducting Oxides *Chemistry of Materials* **16** 5233-5248.

3   Breeze A J *et al* 2001 Charge transport in TiO_2/MEH-PPV polymer photovoltaics *Physical Review B* **64** 125205.

4   Tahar R B H *et al* 1998 Tin doped indium oxide thin films: Electrical properties *J. Appl. Phys.* **83** 2631-2645.

5   Kaspar T C *et al* 2011 ZnO/Sn:In_2O_3 and ZnO/ CdTe Band Offsets for Extremely Thin Absorber Photovoltaics *Appl. Phys. Lett.* **99** 263504.

6   Tang C W and Vanslyke S A 1987 Organic electroluminescent diodes *Appl. Phys. Lett.* **51** 913

7   Tang L-M *et al* 2010 Donor-donor binding in In_2O_3: Engineering shallow donor levels *J. Appl. Phys.* **107** 083704

8   Steele B C H and Golden S J 1991 Variable transmission electrochromic windows utilizing tindoped indium oxide counterelectrodes *Appl. Phys. Lett.* **59** 2357

9   Lee B H *et al* 1997 Effect of process parameters on the characteristics of indium tin oxide thin film for flat panel display application *Thin Solid Films* **302** 25-30

10   Hsu S F *et al* 2005 Highly efficient top-emitting white organic electroluminescent devices *Appl. Phys. Lett.* **86** 253508

11   Himmerlich M *et al* 2012 Surface properties of stoichiometric and defect-rich indium oxide films grown by MOCVD *J. Appl. Phys.* **111** 093704

12   X. Lai *et al* 2010 Ordered Arrays of Bead-Chain-like In_2O_3 Nanorods and Their Enhanced Sensing Performance for Formaldehyde *Chemistry of Materials* **22** 3033-3042

13   Rauf I A 1993 Low Resistivity and High Mobility Tin-Doped Indium Oxide Films *Mater. Lett.* **18** 123−127

14   Palmer G B *et al* 1997 Conductivity and Transparency of ZnO/SnO$_2$-Cosubstituted In$_2$O$_3$ Chem. Mater. **9** 3121−3126.

15   Hoel C A *et al* 2010 High-Pressure Synthesis and Local Structure of Corundum-Type In$_{2-2x}$Zn$_x$Sn$_x$O$_3$ (x ≤ 0.7) *J. Am. Chem. Soc.* **132** 16479−16487.

16   Shannon R D 1966 New High Pressure Phases Having The Corundum Structure *Solid State Commun.* **4** 629-630

17   Nordlund Christensen A *et al* 1967 Hydrothermal Investigation of the Systems In$_2$O$_3$·H$_2$O·Na$_2$O and In$_2$O$_3$·D$_2$O·Na$_2$O. The Crystal Structure of Rhombohedral In$_2$O$_3$ and of In(OH)$_3$ *Act. Chem. Scan.* **21** 1046-1056

18   Prewitt C T *et al* 1969 The C Rare Earth Oxide-Corundum Transition and Crystal Chemistry of Oxides Having the Corundum Structure *Inorg. Chem.* **8** 1985-1993

19   Atou T *et al* 1990 Shock-Induced Phase Transition of M$_2$0$_3$ (M = SC, Y, Sm, Gd, and In)-Type Compounds *J. Solid State Chem.* **89** 378-384

20   Gurlo A *et al* 2003 Polycrystalline Well-Shaped Blocks of Indium Oxide Obtained by the Sol-Gel Method and their Gas-Sensing Properties *Chemistry of Materials* **15** 4377-4383

21   Gurlo A *et al* 2003 Corundum-type indium (III) oxide: formation under ambient conditions in Fe$_2$O$_3$–In$_2$O$_3$ system *Inorg. Chem. Comm.* **6** 569-572

22   Yu D B *et al* 2003 Metastable Hexagonal In$_2$O$_3$ Nanofibers Templated from InOOH Nanofibers under Ambient Pressure *Adv. Funct. Mater.* **13** 497-501

23   Seo W S *et al* 2003 Preparation and Optical Properties of Highly Crystalline, Colloidal, and Size-Controlled Indium Oxide Nanoparticles *Adv. Mater.* **15** 795-797

24   Epifani M *et al* 2004 Ambient Pressure Synthesis of Corundum-Type In$_2$O$_3$ *J. Am. Chem. Soc.* **126** 4078-4079

25   Yu D B *et al* 2004 Synthesis of metastable hexagonal In$_2$O$_3$ nanocrystals by a precursor-dehydration route under ambient pressure *J. Solid State Chem.* **177** 1230-1234

26   Sorescu M *et al* 2004 Nanocrystalline rhombohedral In$_2$O$_3$ synthesized by hydrothermal and postannealing pathways *J. Mat. Sci.* **39** 675-677

27   Lee C H *et al* 2006 Ambient Pressure Syntheses of Size-Controlled Corundum-type In$_2$O$_3$ Nanocubes *J. Am. Chem. Soc.* **128** 9326-9327

28   Chen C *et al* 2006 Ultrathin corundum-type In$_2$O$_3$ nanotubes derived from orthorhombic InOOH: synthesis and formation mechanism *Chem. Commun.* **2006** 4632-4634

29   Xu J Q *et al* 2007 A new route for preparing corundum-type In$_2$O$_3$ nanorods used as gas-sensing materials *Nanotech.* **18** 115615

30   Wang Ch Y *et al* 2008 Phase Stabilization and Phonon Properties of Single Crystalline Rhombohedral Indium Oxide *Cryst. Growth Des.* **8**, 1257-1260

31   Gurlo A *et al* 2008 Nanocubes or Nanorhombohedra? Unusual Crystal Shapes of Corundum-Type Indium Oxide *J. Phys. Chem. C* **112** 9209-9213

32   Gurlo A *et al* 2008 Metastability of Corundum-Type In$_2$O$_3$ *Chem. Eur. J.* **14** 3306-3310

33   Saitoh H *et al* 2008 Solid-phase grain growth of In$_2$O$_3$ at high pressures and temperatures *J. Cryst. Growth* **310** 2295-2297

34   Farvid S S *et al* 2009 Dopant-Induced Manipulation of the Growth and Structural Metastability of Colloidal Indium Oxide Nanocrystals *J. Phys. Chem. C* **113** 15928-15933

35   Farvid S S *et al* 2010 Phase-Controlled Synthesis of Colloidal In$_2$O$_3$ Nanocrystals via Size-Structure Correlation *Chem. Mater.* **22** 9-11

36 García-Domene B *et al* 2014 Pbca-Type In$_2$O$_3$: The High Pressure Post-Corundum Phase at Room Temperature *J. Phys. Chem. C* **118** 20545−20552

37 García-Domene B *et al* 2015 Synthesis and High-Pressure Study of Corundum-Type In$_2$O$_3$ *J. Phys. Chem. C* **119** 29076-29087

38 Bekheet M F *et al* 2015 Kinetic control in the synthesis of metastable polymorphs: Bixbyite-to-Rh$_2$O$_3$(II)-to-corundum transition in In$_2$O$_3$ *J. Solid State Chem.* **229** 278-286

39 Wu M *et al* 2015 Hydrothermal synthesis of porous rh-In$_2$O$_3$ nanostructures with visible-light-driven photocatalytic degradation of tetracycline *CrystEngComm.* **17** 2336-2345

40 Jiang H *et al* 2013 Hierarchical rh-In2O3 crystals derived from InOOH counterparts and their sensitivity to ammonia gas *CrystEngComm.* **15** 7003-7009

41 Karazhanov S Zh *et al* 2007 Phase stability, electronic structure, and optical properties of indium oxide polytypes *Phys. Rev. B* **76** 075129

42 Fuchs F and Bechstedt F 2008 Indium-oxide polymorphs from first principles: Quasiparticle electronic states *Phys. Rev. B* **77** 155107

43 Lu Y-B *et al* 2016 Geometric, electronic and optical properties of zinc/tin codoped In$_2$O$_3$ modulated by the bixbyite/corundum phase transition *J. Phys. D: Appl. Phys.* **49** 065105

44 de Boer T *et al* 2016 Band gap and electronic structure of cubic, rhombohedral, and orthorhombic In$_2$O$_3$ polymorphs: Experiment and theory *Phys. Rev. B* **93** 155205

45 Brazhkin V 2006 Metastable phases, phase transformations, and phase diagrams in physics and chemistry *Physic-Uspekhi* **49** 719-724

46 Jansen M *et al* A 2012 Universal Representation of the States of Chemical Matter Including Metastable Configurations in Phase Diagrams *Angew. Chem. Int. Ed.* **5** 132-135

47	Gurlo A 2010 Structural Stability of High-Pressure Polymorphs in In_2O_3 Nanocrystals: Evidence of Stress-Induced Transition? *Angew. Chem., Int. Ed.* **49** 5610−5612

48	Yusa H *et al* 2008 Rh_2O_3(II)-type structures in Ga_2O_3 and In_2O_3 under high pressure: Experiment and theory *Phys. Rev. B* **77** 064107

49	Gurlo A *et al* 2008 High-pressure high-temperature synthesis of Rh_2O_3-II-type In_2O_3 polymorph *Phys. Stat. Sol. RRL* **2** 269-271

50	Bekheet M F *et al* 2013 Orthorhombic In_2O_3: A Metastable Polymorph of Indium Sesquioxide *Angew. Chem. Int. Ed.* **52** 6531-6535

51	Bekheet M F *et al* 2013 In situ high pressure high temperature experiments in multi-anvil assemblies with bixbyite-type In_2O_3 and synthesis of corundum-type and orthorhombic In_2O_3 polymorphs *High Press. Res.* **33**, 697-711

52	Yusa H *et al* 2008 α-Gd_2S_3-type structure in In_2O_3: Experiments and theoretical confirmation of a high-pressure polymorph in sesquioxide *Phys. Rev. B* **78** 092107

53	Cherian R *et al* 2010 Size dependence of the bulk modulus of semiconductor nanocrystals from first-principles calculations *Phys. Rev. B* **82** 235321

54	Guo D *et al* 2014 Mechanical properties of nanoparticles: basics and applications *J. Phys. D: appl. Phys.* **47** 013001

55	Piot L *et al* 2013 Amorphization in Nanoparticles *J. Phys. Chem C* **117** 11133-11140

56	Machon, D *et al* 2014 Thermodynamics of Nanoparticles: Experimental Protocol Based on a Comprehensive Ginzburg-Landau Interpretation *Nanoletters* **14** 269-276

57	Machon D and Melinon P 2015 Size-dependent pressure-induced amorphization: a thermodynamic panorama *Phys. Chem. Chem. Phys.* **17** 903-910

58   Qi J *et al* 2011 Compression behavior and phase transition of cubic In$_2$O$_3$ nanocrystals *J. Appl. Phys.* **109** 063520

59   García-Domene B *et al* 2012 High-pressure lattice dynamical study of bulk and nanocrystalline In$_2$O$_3$ *J. Appl. Phys.* **112** 123511

60   Tang S X *et al* 2015 Effects of microstructures on the compression behavior and phase transition routine of In$_2$O$_3$ nanocubes under high pressures *RSC Adv.* **5** 85105-85110

61   Singhal A *et al* 2016 Corundum type indium oxide nanostructures: ambient pressure synthesis from InOOH, and optical and photocatalytic properties *RSC Adv.* **6** 108393-108403

62   Dewaele A *et al* 2004 Equations of state of six metals above 94 GPa *Phys. Rev. B* **70** 094112

63   Syassen K 2008 Ruby under pressure *High Press. Res.* **28** 75-126

64   Knapp M *et al* 2011 Technical concept of the materials science beamline at ALBA *Z. Kristallogr. Proc.* **1**, 137-142

65   Hammersley A P *et al* 1996 Two-dimensional detector software: From real detector to idealised image or two-theta scan *High Press. Res.* **14** 235-248

66   Kraus W and Nolze G 1996 POWDER CELL - a program for the representation and manipulation of crystal structures and calculation of the resulting X-ray powder patterns *J. Appl. Crystallogr.* **29** 301-303

67   Toby B H 2001 EXPGUI, a graphical user interface for GSAS *J. Appl. Crystallogr.* **34** 210-213

68   Hohenberg P and Kohn W 1964 Inhomogeneous Electron Gas *Phys. Rev.* **136** B864-B871

69   Kresse G and Hafner J 1993 Ab. initio molecular dynamics for liquid metals *Phys. Rev. B* **47** 558-561

70   Blöchl P E 1994 Projector augmented-wave method *Phys. Rev. B* **50** 17953-17979

71   Perdew J P *et al* 2008 Restoring the Density-Gradient Expansion for Exchange in Solids and Surfaces *Phys. Rev. Lett.* **100** 136406

72   Parlinski K computer code PHONON. See: http://wolf.ifj.edu.pl/phonon.

73   Errandonea D *et al* 2006 Structural transformation of compressed solid Ar: An x-ray diffraction study to 114 GPa *Phys. Rev. B* **73** 092106

74   Errandonea D *et al* 2005 Pressure-induced $\alpha \rightarrow \omega$ transition in titanium metal: a systematic study of the effects of uniaxial stress *Physica B* **355** 116–125

75   Errandonea D *et al* 2012 Compressibility and structural stability of ultra-incompressible bimetallic interstitial carbides and nitrides *Phys. Rev. B* **85** 144103

76   Murnaghan F D 1944 THE COMPRESSIBILITY OF MEDIA UNDER EXTREME PRESSURES *Proc. Natl. Acad. Sci.* **30** 244-247

77   Birch F 1944 Finite Elastic Strain of Cubic Crystals *Phys. Rev.* **71** 809-824

78   Al-Khatatbeh Y *et al* 2012 Compressibility of Nanocrystalline TiO_2 Anatase *J. Phys. Chem. C* **116** 21635-21639

79   Popescu C *et al* 2014 Compressibility and Structural Stability of Nanocrystalline TiO_2 Anatase Synthesized from Freeze-Dried Precursors *Inorg. Chem.* **53** 11598−11603

80   Bouvier P *et al* 2000 High-pressure structural evolution of undoped tetragonal nanocrystalline zirconia *Phys. Rev. B* **62** 8731-8737

81   Ohtaka O *et al* 2002 Phase Relations and EOS of ZrO_2 and HfO_2 Under High-temperature and High-pressure *High Press. Res.* **22** 221-226

82   He Y *et al* 2005 High-pressure behavior of SnO_2 nanocrystals *Phys. Rev. B* **72** 212102

83   Marquardt H *et al* 2011 Elastic properties of MgO nanocrystals and grain boundaries at high pressures by Brillouin scattering *Phys. Rev. B* **84** 064131

84   Jiang J Z *et al* 2000 Structural stability in nanocrystalline ZnO *Europhys. Lett.* **50** 48−53

85   Chen B *et al* 2002 Particle-size effect on the compressibility of nanocrystalline alumina *Phys. Rev. B* **66** 144101

86   Swamy V *et al* 2009 Unusual Compression Behavior of Anatase TiO_2 Nanocrystals *Phys. Rev. Lett.* **103** 075505

87   Sato Y and Akimoto S 1979 Hydrostatic compression of four corundumtype compounds: $αAl_2O_3$, V_2O_3, Cr_2O_3, and $αFe_2O_3$ *J. Appl. Phys.* **50** 5285-5291

88   Besson J M *et al* 1991 High-pressure phase transition and phase diagram of gallium arsenide *Phys. Rev. B* **44** 4214-4234

89   Liu G *et al* 2016 Nanocrystals in compression: unexpected structural phase transition and amorphization due to surface impurities *Nanoscale* **8** 11803-11809

90   Machon, D *et al* 2011 Interface Energy Impact on Phase Transitions: The Case of TiO_2 Nanoparticles *J. Phys. Chem. C* **115** 22286-22291

91   Vilaplana R *et al* 2013 Lattice Dynamics Study of $HgGa_2Se_4$ at High Pressures *J. Phys. Chem. C* **117** 15773-15781

92   Lee C H *et al* 2006 Ambient Pressure Syntheses of Size-Controlled Corundum-type In_2O_3 Nanocubes *J. Am. Chem. Soc.* **128** 9326-9327

93   Yang W *et al* 2013 Coherent diffraction imaging of nanoscale strain evolution in a single crystal under high pressure *Nature Commun.* **4** 1680